ACS APPLIED MATERIALS & INTERFACES

Research Article

www.acsami.org

# Enhancement of the Stability of Electron Field Emission Behavior and the Related Microplasma Devices of Carbon Nanotubes by Coating Diamond Films

Ting-Hsun Chang,[†] Srinivasu Kunuku,[‡] Ying-Jhan Hong,[†] Keh-Chyang Leou,[‡] Tri-Rung Yew,[†] Nyan-Hwa Tai,*[,†] and I-Nan Lin*[,§]

[†]Department of Materials Science and Engineering, National Tsing-Hua University, Hsinchu 300, Taiwan R.O.C

[‡]Department of Engineering and System Science, National Tsing-Hua University, Hsinchu 300, Taiwan R.O.C

[§]Department of Physics, Tamkang University, Tamsui 251, Taiwan R.O.C

**ABSTRACT:** The enhanced lifetime stability for the carbon nanotubes (CNTs) by coating hybrid granular structured diamond (HiD) films on Au-decorated CNTs/Si using a two-step microwave plasma enhanced chemical vapor deposition process was reported. Electron field emission (EFE) properties of HiD/Au/CNTs emitters show a low turn-on field ($E_0$) of 3.50 V/$\mu$m and a high emission current density ($J_e$) of 0.64 mA/cm$^2$ at an applied field of 5.0 V/$\mu$m. There is no notable current degradation or fluctuation over a period of $\tau_{HiD/Au/CNTs}$ = 360 min for HiD/CNTs EFE emitters tested under a constant current of 4.5 $\mu$A. The robustness of the HiD/CNTs EFE emitter is overwhelmingly superior to that of bare CNTs EFE emitters ($\tau_{CNTs}$ = 30 min), even though the HiD/Au/CNTs do not show the same good EFE properties as CNTs, which are $E_0$ = 0.73 V/$\mu$m and $J_e$ = 1.10 mA/cm$^2$ at 1.05 V/$\mu$m. Furthermore, the plasma illumination (PI) property of a parallel-plate microplasma device fabricated using the HiD/Au/CNTs as a cathode shows a high Ar plasma current density of 1.76 mA/cm$^2$ at an applied field of 5600 V/cm with a lifetime of plasma stability of about 209 min, which is markedly better than the devices utilizing bare CNTs as a cathode. The CNT emitters coated with diamond films possessing marvelous EFE and PI properties with improved lifetime stability have great potential for the applications as cathodes in flat-panel displays and microplasma display devices.

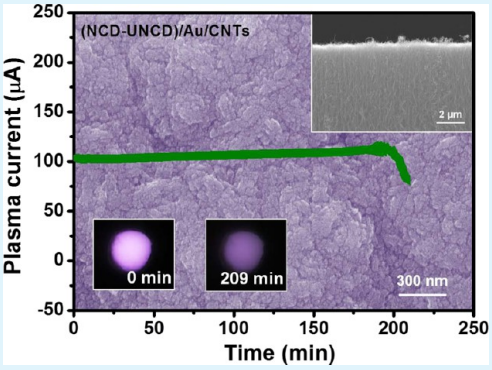


**KEYWORDS:** *hybrid structured diamond films, carbon nanotubes, plasma illumination behavior, electron field emission properties*

## INTRODUCTION

Carbon nanotubes (CNTs) have caught broad research interest since the documented discovery of CNTs in 1991,[1] which is owing to the realization of their high aspect ratio, small tip radius of curvature, excellent electrical and mechanical properties, chemical inertness, and marvelous electron field emission (EFE) properties. CNTs are used as electron sources in devices ranging from flat-panel displays to emitters for electron microscopes.[2−5] However, the short lifetime and the poor stability of the CNT emitters have been the major barriers averting their profitable viability.[6] The EFE properties are easily degraded, since the tips of CNTs are susceptible to ion bombardment erosion by the residual gases in the devices.[7] To surmount this deficiency, CNTs have been combined with other field emitting materials by depositing a thin film on CNTs,[8−11] decorating CNTs with nanoparticles,[12] or by making composites of CNTs.[13,14]

On the contrary, diamond has the strongest bonded structure and excellent physical and chemical properties, which makes the diamond strongly competing with cold cathode materials for EFE applications.[15−17] Diamond could operate for a long lifetime with high reliability. Furthermore, diamond can be utilized at high temperature or high power due to high electrical breakdown field and high thermal conductivity properties, which are highly advantageous over other materials. On the basis of the high robustness of diamond films and significant EFE properties of CNTs, it is interesting to integrate these two carbon materials to attain highly stable EFE characteristics.

Recently, many attempts have been made to couple the diamond and CNTs,[10,11,18−20] but the results are still not satisfactory, which is probably due to the difficulty in the integration of these two materials. Zou et al.[10] have grown diamond-coated CNTs, showing teepee-shaped structures, by hot filament chemical vapor deposition. Sun et al.[19] have performed structural phase transformation from multiwalled CNTs (MWCNTs) to nanocrystalline diamond by hydrogen plasma post-treatment. Xiao et al.[20] have grown a hybrid nanocarbon material consisting of ultrananocrystalline diamond (UNCD) and MWCNTs by selectively patterning a Si(100) substrate precoated with diamond nanoparticle seeds and

Received: April 17, 2014
Accepted: June 23, 2014
Published: June 23, 2014

  

catalysts, followed by microwave plasma enhanced chemical vapor deposition (MPE-CVD) for the growth of UNCD and MWCNTs. Moreover, among the diamond films with a hybrid granular structure, the HiD films, obtained by growing the nanocrystalline diamond (NCD) on a UNCD seeding layer, possess marvelous EFE properties and are most appropriate for the development of diamond−CNTs composite EFE emitters.

In this work, we sythesized the HiD films on CNTs using a two-step MPE-CVD process and investigated their EFE properties. The achieved EFE behavior is comparable to that of bare CNTs, but with superior lifetime stability. Such an observation demonstrated that these HiD-coated CNTs can potentially be used in EFE-based devices. Additionally, we also demonstrated the advantage of these HiD-coated CNTs over the bare CNTs, which were used as the cathode for a microplasma device for enhancing the performance of the device.

## EXPERIMENTAL METHODS

The CNTs were grown on Si substrates, using $C_2H_2$ as carbon sources and Fe nanoclusters as catalysts, in a thermal chemical vapor deposition process (750 °C, 10 min). The Fe nanoclusters were obtained from the thermal annealing (750 °C, 5 min) of a thin Fe coating (∼2 nm) on Si substrates. Prior to the growth of diamond films, the CNTs were decorated with nanosized diamond particulates by the electrophoresis deposition (EPD) process, which has been described in detail elsewhere.[21] In the EPD process, the single-digit diamond particulates (Plasma Chem) aqueous solution with a concentration of 0.1 g/L was used. The CNTs/Si substrates were biased at approximate +20 V with respect to the Pt reference electrode, and the EPD process was performed for 30 s. The UNCD films were first grown on the CNTs by using a MPE-CVD system (2.45 GHz, IPLAS-CYRANNUS) in a $CH_4$(4%)/Ar plasma with a microwave power of 1200 W for 60 min. The pressure and the total flow rate were maintained at 120 Torr and 100 sccm, respectively. Subsequently, a layer of NCD film was grown on top of UNCD/CNTs by the secondary MPE-CVD process using a $CH_4$/Ar(49%)/$H_2$(50%) plasma with 80 Torr chamber pressure and 1300 W microwave power for 60 min to obtain a diamond film with a hybrid granular structure, the HiD film. No external heater was used to heat the substrate. The substrate temperature was increased due to the plasma bombardment heating up to around 450−470 °C, which was monitored by a thermocouple embedded in the stainless steel substrate holder. Thus, the obtained samples were designated as UNCD/CNTs or HiD/CNTs.

The morphology and the microstructure of the bare CNTs, UNCD/CNTs, and HiD/CNTs were examined using a scanning electron microscope (SEM, JEOL-6500) and a high-resolution transmission electron microscope (HRTEM; JEOL-2100F operated at 200 kV), respectively. The bonding structure of the bare CNTs, UNCD/CNTs, and HiD/CNTs was characterized by a UV-Raman spectroscope (Lab Raman HR800, Jobin Yvon, $\lambda$ = 325 nm). The EFE properties of the bare CNTs, UNCD/CNTs, and HiD/CNTs were measured using a parallel-plate setup, in which the diamond films coated CNTs were used as cathodes and the indium tin oxide (ITO) glass coated with phosphor was used as an anode. The anode-to-cathode separation was fixed by a polytetrafluoroethylene (PTFE) spacer with a thickness of 200 $\mu$m. The current−voltage ($I$−$V$) characteristics of EFE properties were measured using an electrometer (Keithley 2410) under pressure below $10^{-6}$ Torr, and the $I$−$V$ charactersitcs were analyzed by the Fowler−Nordheim theory.[22]

The plasma illumination (PI) characteristics of a microplasma device using bare CNTs, UNCD/CNTs, or HiD/CNTs as cathodes were also investigated. In the microplasma devices, the glass coated with ITO was used as an anode and the anode-to-cathode separation was fixed by a PTFE spacer (1.0 mm in thickness). A circular hole about 3.0 mm in diameter was cut out from the PTFE spacer to form a microcavity. The device was connected through a circiut with two 1 MΩ resisters in parallel, and the plasma was triggered using a direct current voltage source. The chamber was evacuated to reach a base pressure of 0.1 mTorr and then purged with Ar for 10 min (in 2 Torr). The Ar gas was channeled into the chamber at a flow rate of 10 sccm throughout the measurements. The plasma current versus applied voltage characteristics were measured using an electrometer (Keithley 237).

## RESULTS AND DISCUSSION

Figure 1a,b shows the cross-sectional and top-view SEM morphologies, respectively, of the CNTs used to grow the diamond films. The CNTs were completely etched out by the $CH_4$/Ar plasma during the growth UNCD process in the MPE-CVD system. To solve the difficulty in growing diamond on CNTs by the MPE-CVD process, we utilized the EPD process[21] to precoat nanodiamond particulates (∼10 nm in size) on the top of CNTs to protect them from the damage due to Ar-ion bombardment. Figure 1c shows the top-view SEM micrograph for CNTs after the decoration of nanodiamond particulates.

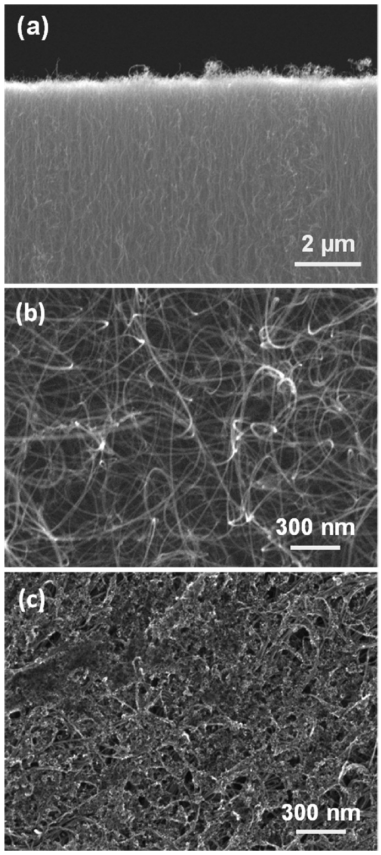


**Figure 1.** (a) The cross-sectional and (b) the top-view SEM micrographs of the vertically aligned CNTs grown on Si substrates (the CNTs are about 100 $\mu$m in length). (c) The top-view SEM micrographs of the vertically aligned CNTs, which were decorated with nanodiamond particulates.

The decoration of nanodiamond particulates on CNTs not only increased the durability of CNTs in $CH_4$/Ar plasma but also facilitated markedly the nucleation of the diamond. Figure 2a shows that the UNCD films were grown easily on top of CNTs, using a $CH_4$(4%)/Ar plasma, fully covered nanodiamond decorated CNTs. The cross-sectional image of UNCD/CNTs is shown as the inset in Figure 2a. It should be noted that the nucleation and growth behavior of UNCD

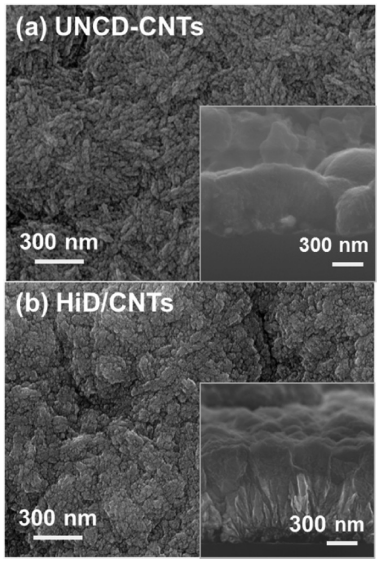


**Figure 2.** SEM micrographs of the diamond-coated CNTs: (a) UNCD/CNTs with the cross-sectional image of UNCD/CNTs shown as the inset and (b) HiD/CNTs with the cross-sectional image of HiD/CNTs shown as the inset.

films on nanodiamond decorated CNTs is very much different from that on planar Si substrates. Usually, when the planar Si substrates were pretreated with the proper nucleation process, such as ultrasonication in nanodiamond containing methanol solution, the UNCD films can be grown readily in $CH_4$/Ar plasma. Successful growth of UNCD films on Si substrates has been observed for $CH_4$/Ar plasma with $CH_4$ content in growth plasma varying from 0.5% to 10%. However, in the case of nanodiamond decorated CNTs, no diamond films were observed when the $CH_4$ content in the $CH_4$/Ar plasma is smaller than a critical value, i.e., 4%, because the CNTs were etched out in the plasma containing a too low percentage of $CH_4$. When the $CH_4$ content is larger than the critical value, the UNCD films grew nicely, fully covering the CNTs. The morphologies of the UNCD films grown on top of nanodiamond decorated CNTs are similar to those of the conventional UNCD films grown on Si substrates; i.e., they contain nanosized diamond grains with very smooth surfaces (figures not shown).

After the successful growth of UNCD films on CNTs, the subsequent growth of NCD films on top of the UNCD/CNTs films is straightforward. Notably, the purpose of growing NCD films on top of the UNCD seeding layer using $CH_4$(1%)/Ar(49%)/$H_2$(50%) plasma is to modify the granular structure of the UNCD layer, as explained in our previous studies,[23,24] revealing that the secondary MPE-CVD process preferentially etched out the *trans*-polyacetylene phase in the grain boundaries and triggered the coalescence process for nanosized diamond grains and, in the meantime, induced the formation of nanographitic clusters. Such a two-step process formed a HiD film containing large diamond aggregates dispersed evenly among the matrix of nanosized diamond grains, resulting in superior EFE properties, which is even better than the UNCD films. The typical SEM morphology and cross-sectional SEM of the HiD/CNT films are shown in Figure 2b and the inset in Figure 2b, respectively, indicating the formation of a cauliflower-like morphology with the size of approximately 100 nm.

Contrary to a single G-band at 1580 $cm^{-1}$ for CNTs (curve I, Figure 3), UV Raman spectra shown in Figure 3 (curve II)

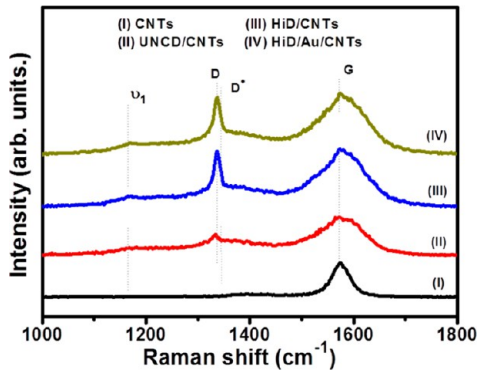


**Figure 3.** Raman spectroscopy of (I) CNTs, (II) UNCD/CNTs, (III) HiD/CNTs, and (IV) HiD/Au/CNTs.

corresponding to the UNCD/CNTs materials indicate that there are several Raman resonance peaks observable for these films. There is a small D-band resonance peak at 1332 $cm^{-1}$,[25] representing diamond. In addition, there are a diffuse D*-band (~1350 $cm^{-1}$) and a G-band (~1580 $cm^{-1}$), representing disordered carbon and graphite phase, respectively. The $\nu_1$-band (1140 $cm^{-1}$),[26,27] representing the grain boundary phase designated as *trans*-polyacetylene, is the one that could be barely observable. The Raman characteristics of UNCD/CNTs are similar to those of UNCD grown on Si substrates (not shown). The broadness of the Raman resonance peaks is presumably owing to the smallness of the diamond grains in the UNCD films. Curve III in Figure 3 shows that the HiD/CNT films contain a large and sharp D-band (at 1332 $cm^{-1}$) along with other diffused smaller resonance peaks, implying the coexistence of large and ultrasmall diamond grains. The presence of a strong G-band resonance peak near 1580 $cm^{-1}$ is presumably contributed from the underlying CNTs.

The microstructure of the HiD/CNTs was investigated using TEM. Notably, in the preparation of the TEM thin foil, the samples can be either ion-milled from the Si side to form a thin foil mainly containing the surface region of the HiD/CNT materials (designated as "surface region") or ion-milled from the diamond side to form a thin foil mainly containing the region near the HiD-to-CNTs interface (designated as "interface region"). Figure 4a shows that the "surface region" of the HiD/CNTs materials contains some large aggregates evenly distributed among the matrix of ultrasmall diamond grains. The detailed microstructure of the large aggregates (region "I", Figure 4a) is illustrated using the TEM structure image depicted in Figure 4b. This micrograph and the associated Fourier transformed diffractogram $FT_{0b}$ (inset, Figure 4b) show that the aggregate is of diamond materials, containing a large proportion of planar defects, which is indicated by the presence of streaks and a systematic row of diffraction spots in the $FT_{0b}$ image. The $ft_1$ shows the FT images corresponding to region 1 in Figure 4b. The presence of the planar defects is highlighted by area 2 and the associated FT image ($ft_2$) in Figure 4b. On the other hand, the TEM image corresponding to the ultrasmall grains region, which is adjacent to the large diamond aggregates (region "II", Figure 4a), is shown in Figure 4c, implying that this region contains abundant nanosized clusters ranging from 5 to 10 nm. The FT image ($FT_{0c}$, inset of Figure 4c) clearly illustrates that these nanosized

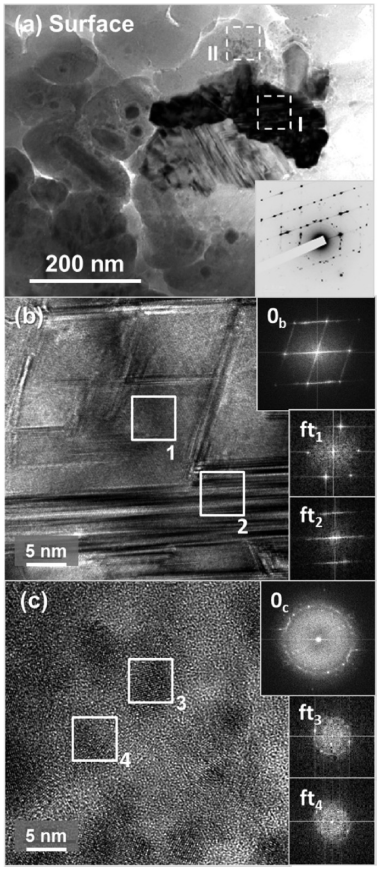


**Figure 4.** (a) The TEM bright-field image of the "surface region" of the HiD/CNTs films with the inset showing the SAED. (b) The enlarged TEM image of the large aggregated (region I in "a") with the inset $FT_{0b}$ showing the FT image corresponding to the whole structure image in "b", and the $ft_1$ and $ft_2$ show the FT images corresponding to regions 1 and 2, respectively. (c) The enlarged TEM image of the small grain region (region II in "a") with the inset $FT_{0c}$ showing the FT image corresponding to the whole structure image in "c", and the $ft_3$ and $ft_4$ show the FT images corresponding to regions 3 and 4, respectively.

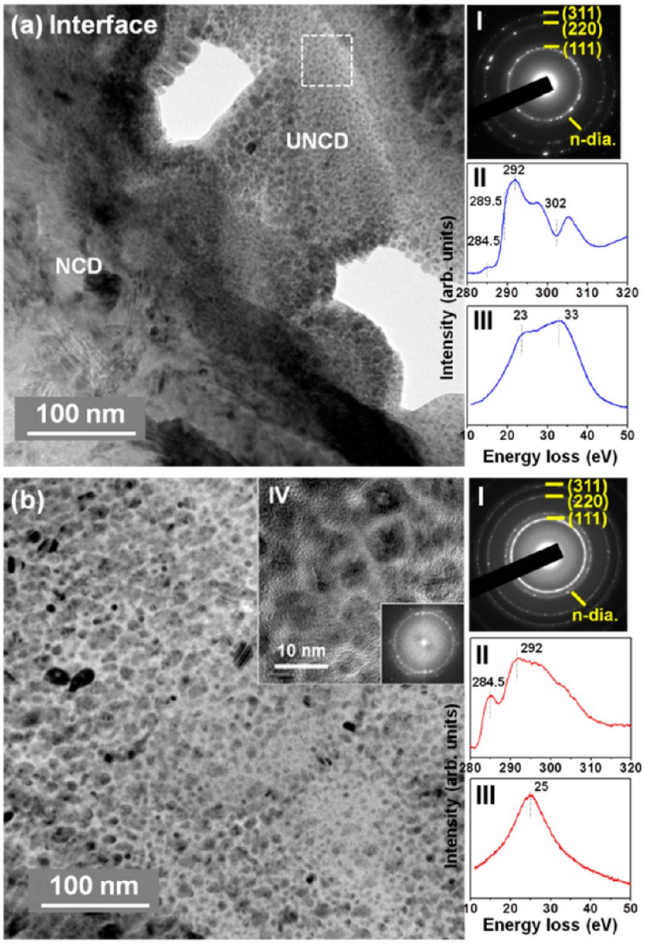


**Figure 5.** (a) The TEM bright-field image of the "interface region" of the HiD/CNTs films with the inset I showing the SAED and the insets II and III showing the core-loss and plasmon-loss EELS spectra, respectively. (b) The enlarged TEM micrograph of the region designated as dashed square in "a" with the inset I showing the SAED and the insets II and III showing the core-loss and plasmon-loss EELS spectra, respectively. The inset IV shows the TEM structure image of a typical region in "b".

clusters are diamond. Moreover, this region contains a large proportion of $sp^2$-bonded carbons, indicated by the presence of a large diffuse diffraction ring in the center of the $FT_{0c}$ image. Apparently, the presence of a $sp^2$-bonded phase among the boundaries of the small diamond grains formed a conducting network, facilitating the transport of electrons, which is the prime factor rendering HiD materials to exhibit overwhelmingly superior EFE properties compared with the UNCD films.

In contrast, Figure 5 shows the microstructure of the "interface region", which is underneath the "surface region". Although the TEM bright-field image in Figure 5a does not clearly reveal the existence of diamond grains, the selective area electron diffraction (SAED) shown in inset I of Figure 5a clearly indicated the presence of the $(111)_{dia}$, $(220)_{dia}$, and $(311)_{dia}$ diffraction rings, implying that these materials contained mostly diamond. It is interesting to note that there appears a prominent diffraction ring with the size slightly larger than the $(111)_{dia}$, which corresponds to *n*-diamond, an allotropy of the *Fm*3*m* structured diamond.[28−30] It should be noted that the *n*-diamond has carbon atoms arranged in FCC lattices, which can be viewed as a diamond structure with some carbon atoms missing, and is presumed to be the materials formed prior to the nucleation of diamond from the carbon matrix.[28−30] The core-loss electron energy loss spectroscopy (EELS) (inset II in Figure 5a) indicates the presence of a $\sigma^*$-band near 289.5 eV with a deep valley near 302 eV, further confirming that this region was predominated with the $sp^3$-bonded carbon, diamond.[31,32] The plasmon-loss EELS (inset III, Figure 5a) shows a peak at 33 eV with a shoulder near 23 eV. The peak at 33 eV corresponds to the bulk plasma of the nanosized diamond cluster, whereas the shoulder near 23 eV corresponds to the suface plasma of the diamond clusters.[28,33] These plasmon-loss EELS further confirm that the materials in this region contain mostly diamond.

Figure 5b shows the enlarged TEM micrograph of the interface region, which is marked by a dashed square in Figure 5a, indicating that this region contains abundant clusters. The granular structure of the clusters is not clearly resolvable. The SAED shown as inset I in Figure 5b contains a prominent *n*-diamond diffraction ring besides the $(111)_{dia}$, $(220)_{dia}$, and $(311)_{dia}$ diamond diffraction rings. There is large intensity of a central diffuse diffraction pattern, implying the existence of a large proportion of $sp^2$-bonded carbon, including amorphous or graphitic phases in this region. Moreover, the TEM structure

image shown in inset IV of Figure 5b and the associated FT image (inset of inset IV) revealed again that this region contains mostly the *n*-diamond clusters (the ring-shaped diffraction pattern) with some proportion of $sp^2$-bonded carbon (the central diffuse ring). The core-loss EELS shown as inset II in Figure 5b is predominated with the $\pi^*$-band near 284.5 eV, the peak at ~292 eV that corresponds to transitions from the 1s to the $\sigma^*$ states, which is presumably contributed by the underlying CNT materials. The sign of diamond ($\sigma^*$-band at 289.5 eV and deep valley at 302 eV) was not clearly observable. The plasmon-loss EELS (inset III, Figure 5b) shows a single peak near 25 eV, confirming that the $sp^2$-bonded materials contained in this region are the graphitic phase. Such an observation inferred that the nucleation of diamond on top of CNTs started with the formation of the graphitic phase, followed by the nucleation of *n*-diamond nanocrystals among the graphitic phase.

Figure 6a shows the EFE properties, the $J-E$ curves, of the materials, whereas Figure 6b indicates the corresponding Fowler–Nordheim (F–N) plots. From the interception of the straight line segments of the F–N plots, the turn-on field ($E_0$) of the EFE process was determined. The CNTs possess very good EFE and PI properties. Curves labeled I of Figure 6a,b show that the EFE process for CNTs can be turned on at $(E_0)_{CNTs}$ = 0.73 V/$\mu$m and the EFE current density ($J_e$) reached a large value of 1.10 mA/cm$^2$ at an applied field of 1.05 V/$\mu$m. However, even though the CNTs possess extremely good EFE properties, they suffer from short lifetimes. Curve I in Figure 6c shows that the lifetime of CNT emitters is as short as 30 min, when tested under the condition of 4.5 $\mu$A (0.18 mA/cm$^2$) in $10^{-6}$ Torr. These EFEs are summarized in Table 1.

On the contrary, curve II in Figure 6a shows that, for UNCD/CNTs films, the EFE process can be turned on at $(E_0)_{UNCD/CNTs}$ = 4.90 V/$\mu$m, attaining a large EFE current density of $(J_e)_{UNCD/CNTs}$ = 0.23 mA/cm$^2$ at an applied field of 6.5 V/$\mu$m (curve II). Although these EFE properties are inferior to those of CNT emitters (curve I in Figure 6a), they are still markedly better than those of the UNCD films grown directly on Si substrates [$(E_0)_{UNCD/Si}$ = 16.86 V/$\mu$m].

Moreover, using the HiD films to replace the UNCD films in diamond–CNTs composites markedly enhanced the EFE properties. The HiD/CNT films show superior EFE properties (curve III, Figure 6a) to the UNCD/CNTs, i.e., $(E_0)_{HiD/CNTs}$ = 3.89 V/$\mu$m, with $(J_e)_{HiD/CNTs}$ = 0.53 mA/cm$^2$ at an applied field of 5.3 V/$\mu$m. The HiD/CNTs emitters exhibit markedly longer lifetimes, compared with those based on CNTs, although HiD/CNT films do not show as good EFE properties as CNTs. Curve II in Figure 6c reveals that, when the lifetime was tested at 4.5 $\mu$A (0.18 mA/cm$^2$), the HiD/CNT emitters can last $\tau_{HiD/CNTs}$ = 275 min without showing any sign of decaying in EFE characteristics, compared with the short lifetime of CNTs ($\tau_{CNTs}$ = 30 min, curve I in Figure 6c). Obviously, the two-step MPE-CVD process, which converted ultrasmall grain microstructured UNCD films into HiD films, not only enhanced the EFE but also improved the robustness of the corresponding devices. It is noteworthy that the robustness of the EFE emitters is of more concern from the viewpoint of practical applications.

To further enhance the EFE of the diamond/CNTs materials, the CNTs were precoated with a thin Au layer (~5 nm) prior to the decoration of nanodiamond particulates for benefitting the growth of HiD films. Curve IV in Figure 6a shows that the $E_0$ was further reduced to $(E_0)_{HiD/Au/CNTs}$ = 3.50

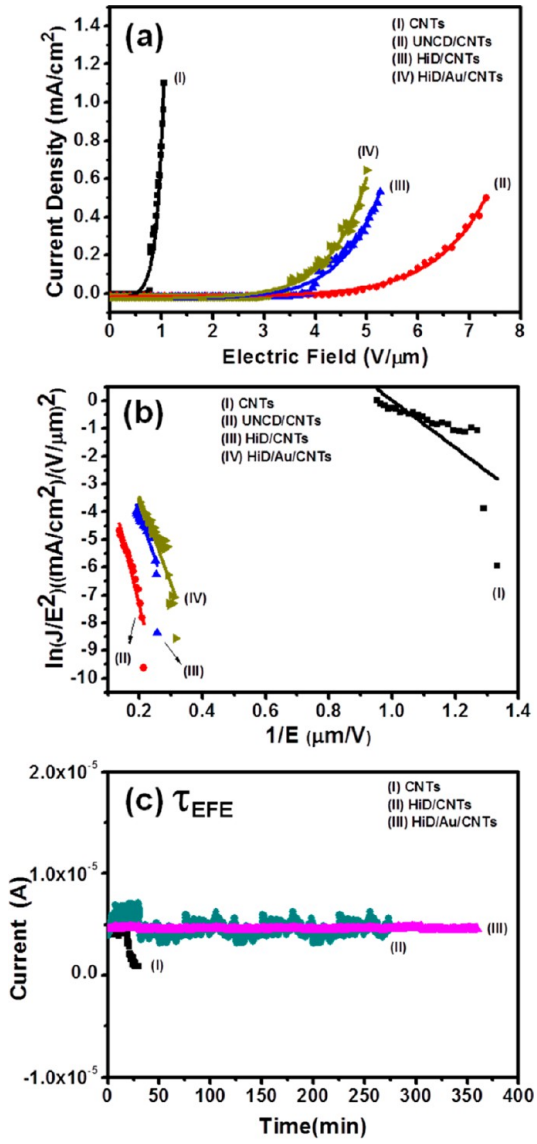


**Figure 6.** (a) The electron field emission properties, $J-E$ curves, and (b) the Fowler–Nordheim plots, i.e., $\ln(J_e/E^2)-1/E$ plots), of (I) CNTs, (II) UNCD/CNTs, (III) HiD/CNTs, and (IV) HiD/Au/CNTs. (c) The lifetime test at 4.5 $\mu$A for the (I) CNTs, (II) HiD/CNTs, and (III) HiD/Au/CNTs EFE emitters.

V/$\mu$m and the EFE current density was increased to $(J_e)_{HiD/Au/CNTs}$ = 0.64 mA/cm$^2$ at an applied field of 5.0 V/$\mu$m. In addition, the EFE current density of HiD/Au/CNTs increased more steadily versus the applied field, compared with the $J_e-E$ behavior of HiD/CNT materials. The most beneficial effect due to the utilization of the Au interlayer is the enhancement in stability of the EFE emitters. Figure 6c shows that the utilization of the Au interlayer increased the lifetime of the EFE emitters markedly, from 275 min for HiD/CNTs to 360 min for HiD/Au/CNTs, before the onset of decaying.

On the other hand, Figure 7 shows that, for the microplasma devices using CNTs as a cathode, the plasma can be ignited at a low voltage of 360 V, which corresponds to a threshold field of $(E_{pl})_{CNTs}$ = 3600 V/cm. The brightness of the plasma increased monotonically with the applied voltage. Such a characteristic is better illustrated by the plasma current density–applied field ($J_{pl}-E$) curves in Figure 8a (curve I), which indicates that the $J_{pl}$ value increased from 0.45 mA/cm$^2$ at an applied field of


dx.doi.org/10.1021/am502330v | ACS Appl. Mater. Interfaces 2014, 6, 11589–11597

**Table 1. EFE and PI Characteristics of CNTs, UNCD/CNTs, HiD/CNTs, and HiD/Au/CNTs Composite Materials**

| | EFE properties | | | | plasma illumination properties | | |
|---|---|---|---|---|---|---|---|
| materials | $^{a}E_0$ (V/$\mu$m) | $^{b}J_e$ (mA/cm$^2$) | $^{c}\tau_{efe}$ (min) | $^{d}(E_{th})_{pl}$ (V/cm) | $^{e}J_{pl}$ (mA/cm$^2$) | $^{f}n_e$ ($10^{14}$·cm$^{-3}$) | $^{g}\tau_{pl}$ (min) |
| CNTs | 0.73 | 1.10@1.05 | 30 | 3600 | 1.86 | 1.34 | 60 |
| UNCD/CNTs | 4.90 | 0.23@6.5 | | 4000 | 1.52 | 1.08 | |
| HiD/CNTs | 3.89 | 0.53@5.3 | 275 | 3800 | 1.62 | 1.16 | 175 |
| HiD/Au/CNTs | 3.50 | 0.64@5.0 | 360 | 3600 | 1.76 | 1.25 | 209 |

$^{a}E_0$: the turn-on field for inducing EFE process, which was designated as the interception of the straight line segments extrapolated from the low field and high field of F−N plots. $^{b}J_e$: the EFE current density at the designated applied field in V/$\mu$m. $^{c}\tau_{efe}$: the lifetime measured at applied current of 4.5 $\mu$A (0.18 mA/cm$^2$). $^{d}(E_{th})_{pl}$: the threshold field for igniting the plasma in parallel-plate microplasma devices. $^{e}J_{pl}$: the plasma current density in parallel-plate microplasma devices measured at an applied field of 5600 V/cm. $^{f}n_e$: the plasma density, which is also the electron density in the parallel-plate microplasma devices, measured at an applied field of 5600 V/cm. $^{g}\tau_{pl}$: the lifetime measured at 100 $\mu$A (1.41 mA/cm$^2$) applied current in parallel-plate microplasma devices.

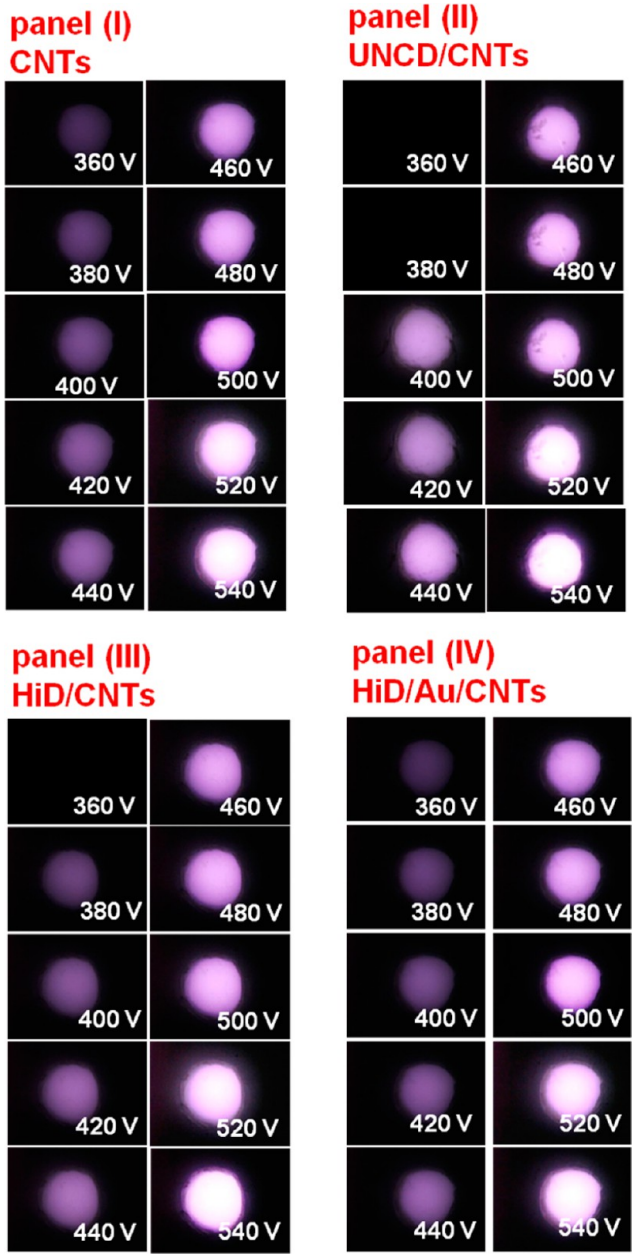


**Figure 7.** Plasma illumination images of a microplasma, which uses panel (I) CNTs, panel (II) UNCD/CNTs, panel (III) HiD/CNTs, and panel (IV) HiD/Au/CNTs as cathodes.

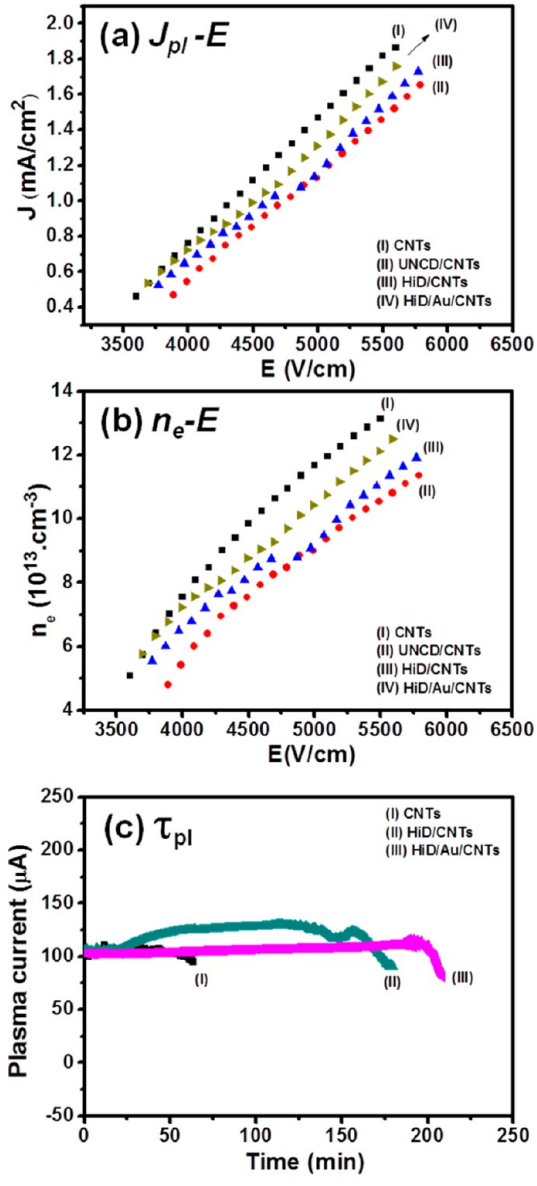


**Figure 8.** (a) Plasma current density vs applied field ($J_{pl}$−$E$) and (b) plasma density vs applied field ($n_e$−$E$) characteristics for of (I) CNTs, (II) UNCD/CNTs, (III) HiD/CNTs, and (IV) HiD/Au/CNTs. (c) The lifetime test (at 100 $\mu$A) for a microplasma device (at 100 $\mu$A) using (I) CNTs, (II) HiD/CNTs, and (III) HiD/Au/CNTs as cathodes.


dx.doi.org/10.1021/am502330v | ACS Appl. Mater. Interfaces 2014, 6, 11589−11597

3600 V/cm to around 1.86 mA/cm$^2$ at 5600 V/cm. From each $J_{pl}$ value, we can calculate the corresponding plasma density, which is the same as the electron density ($n_e$) for the plasma, by using eqs 1−3[34]

$$n_e = \frac{J_{pl}}{E\mu_e e} \quad (1)$$

where $J_{pl}$ is plasma current density, $E$ is applied electric filed, $e$ is electron charge, and $\mu_e$ is electron mobility, which can be calculated by the Einstein relation

$$\frac{D}{\mu_e} = \frac{\kappa T_e}{e} \quad (2)$$

where $\kappa$ ($1.38 \times 10^{-23}$) is the Boltzmann constant, $T_e$ is the electron temperature, and $D$ is the diffusion coefficient, which can be estimated from the empirical formula

$$D = \frac{K \times 10^5}{p} \quad (3)$$

where $p$ is pressure and $K$ is 6.3 for Ar gas.[34] By using computational fluid simulation, we have estimated $T_e$ = 2 eV for pressure ranging from 2 to 100 Torr. Figure 8b shows that the plasma density of the CNT cathode ($(n_e)_{CNTs}$) also increased monotonously versus the applied field, reaching a value of 1.34 × $10^{14}$ cm$^{-3}$ at an applied field of 5600 V/cm. Again, even though the CNT-based microplasma devices possess superior PI behavior, they suffer from shorter lifetimes. Curve I in Figure 8c indicates that the microplasma devices using CNTs as a cathode can last only for 60 min when they were tested in the condition of 100 $\mu$A (1.41 mA/cm$^2$) under a pressure of 2 Torr in an Ar atmosphere.

The UNCD/CNTs-based microplasma devices need a slightly larger applied voltage [$(V_{pl})_{UNCD/CNTs}$ = 400 V, $(E_{pl})_{UNCD/CNTs}$ = 4000 V/cm] to ignite the plasma (Figure 7, panel II) with smaller plasma current density [$(J_{pl})_{UNCD/CNTs}$ = 1.52 mA/cm$^2$ at 5600 V/cm, also curve II in Figure 8a], as compared with those for the CNT-based devices. However, these PI performances are still better than those using UNCD/Si films as cathodes [$(E_{pl})_{UNCD/Si}$ = 4000 V/cm]. Similarly, by using eqs 1−3, $n_e$, the plasma density corresponding to a specific $J_{pl}$ value, can be calculated; and the $n_e$−$E$ curve of the UNCD/CNTs-based microplasma device is shown by curve II in Figure 8b, revealing that the $n_e$ values reach around ∼1.08 × $10^{14}$ cm$^{-3}$ at an applied field of 5600 V/cm. The panel III in Figure 7 shows that the HiD/CNTs-based microplasma can be ignited at lower voltage (380 V), which corresponds to a threshold field of $(E_{pl})_{HiD/CNTs}$ = 3800 V/cm, with a plasma current of $(J_{pl})_{HiD/CNTs}$ = 0.5 mA/cm$^2$ at an applied field of 3800 V/cm (curve III, Figure 8a). The plasma current density ($J_{pl}$) and the plasma density ($n_e$) increased monotonously with applied field, attaining a large plasma current density value of $(J_{pl})_{HiD/CNTs}$ = 1.62 mA/cm$^2$ (curve III, Figure 8a) and a large plasma density value of $(n_e)_{HiD/CNTs}$ = 1.16 × $10^{14}$ cm$^{-3}$ (curve III, Figure 8b) at an applied field of 5600 V/cm. These PI parameters are also summarized in Table 1. Moreover, panel IV in Figure 7 shows that the plasma illumination behavior of the device using HiD/Au/CNTs as a cathode is similar to that of the one using HiD/CNTs as a cathode. However, further detailed analysis of plasma current density vs applied field ($J_{pl}$−$E$) revealed that utilization of the Au interlayer improved slightly the $J_{pl}$−$E$ behavior. The $J_{pl}$ value not only increased more steadily against the applied field but also reached a larger value, i.e., $J_{pl}$ = 1.76 mA/cm$^2$ (curve IV, Figure 8a) with the large $n_e$ value of $n_e$ = 1.25 × $10^{14}$ cm$^{-3}$ (curve IV, Figure 8b) at an applied field of 5600 V/cm.

However, the most noticeable beneficial effect of coating the diamond films on CNTs is the marked improvement in the robustness of the emitters. Figure 8c shows that the HiD/CNTs-based microplasma devices possess significantly better stability. Curve II in Figure 8c indicates that the HiD/CNTs-based microplasma devices can be operated at 100 $\mu$A (1.41 mA/cm$^2$) for $(\tau_{pl})_{HiD/CNTs}$ = 175 min before starting to decay, which is overwhelmingly superior to the CNT-based microplasma devices ($(\tau_{pl})_{CNTs}$ = 60 min, curve I, Figure 8b). Moreover, curve III in Figure 8c indicates that the microplasma devices using HiD/Au/CNTs materials as cathodes last even longer, i.e., 209 min for HiD/Au/CNTs cathode devics.

How the presence of the Au interlayer between the HiD and CNTs can markedly enhance the EFE and the PI behaviors is not totally clear yet. Although using the Au interlayer can markedly enhance the efficiency for the nucleation of diamond nuclei and improve the EFE properties of the UNCD films grown on Si substrates,[35,36] such a mechanism cannot be applied to the HiD/CNTs case, as the Au interlayer is expected not to interdiffuse with the CNTs. The possible explanation is that the Au coating, which formed nanodots sitting on the top of CNTs, improved the adhesion of nanosized diamond particulates and, therefore, facilitated the formation of diamond nuclei on top of the CNTs.

The properties of the as-fabricated EFE and the PI devices are relevant to each other because they adopted the same UNCD films as the cathode materials. Even though we did not fully understand how the EFE properties affect the plasma illumination performance; it is clear that gas discharge takes place under the following four factors, including EFE electrons from cathodes, photoionization, cosmic rays, and radioactive elements. Obviously, the EFE of electrons from the cathode is the mechanism for gas discharge because the measurement of EFE property was carried out in a closed system without applying light and radiation. Moreover it should be mentioned that the threshold field, $(E_{th})_{pl}$, required to trigger the Ar plasma for the microplasma devices using diamond as a cathode is perceptibly smaller than the turn-on field, $(E_0)_{EFE}$, for inducing the EFE process of the corresponding UNCD/CNTs diamond films (cf. Table 1; $(E_{th})_{pl}$ = 4000 V/cm and $(E_0)_{efe}$ = 4.90 V/$\mu$m)). Such a phenomenon is due to different mechanisms for igniting the plasma in an Ar environment (tens of torr) and for turning on the EFE process in a high-vacuum environment ($10^{-6}$ Torr). In a microplasma device, the plasma can be ignited when the electrons emitted from the cathode (primary electron) gain sufficient kinetic energy by applying an electric field to ionize the gas molecules (e.g., 15.7 eV for Ar). Once the primary electrons ionize the Ar gases, the Ar gases become $Ar^+$ ions, which accelerate in sheath fields and move toward cathode. The high-energy $Ar^+$ ions bombard the cathode surface and eject secondary electrons, which play the most important role in maintaining stable discharges due to cascade ionization. Therefore, it seems that the low EFE turn-on field for the HiD/CNT film is not helpful in lowering the threshold field of plasma ignition as compared with those for UNCD/CNTs. However, when the plasma was ignited, there formed a plasma sheath in the vicinity of the cathode where the electric field was markedly increased. For typical plasma with the sheath around 10 $\mu$m in thickness,[37] the electric field

experienced by the cathode will increase to around 40 V/$\mu$m under an applied voltage of 400 V. Such a field is far larger than the turn-on field of the EFE process for most of the diamond films. A large number of electrons will be emitted from the diamond cathode due to bombardment of $Ar^+$ gases on the diamond cathode, inducing secondary electrons that ionized the rest of the Ar gases, as a result, producing cascade electrons and subsequently enhancing the plasma current density. This is the reason why a larger $J_{pl}$ is observed when the HiD/CNT films were used to replace UNCD/CNTs as cathodes (cf. Table 1).

## CONCLUSIONS

In conclusion, we demonstrated a facile and a reproducible way of synthesizing HiD films on CNTs with long lifetime stability of EFE and PI performances, thus overcoming the poor stability of CNT field emitters. The HiD/CNTs (or HiD/Au/CNTs) emitters exhibit an excellent EFE lifetime stability of $\tau_{efe}$ = 275 (or 360) min, when tested at an applied current of 4.5 $\mu$A ($\tau_{efe}$ = 30 min for CNTs emitters). In addition, for HiD-based microplasma devices, the plasma current of 100 $\mu$A is upheld for a period of over 175 (or 209) min, showing better plasma stability compared with that of bare CNT-based ones ($\tau_{pl}$ = 60 min). The present approach of synthesizing HiD/CNT (or HiD/Au/CNT) materials is a direct and simple process that provides a solution for the fabrication of functional field emission devices and opens new prospects of high-definition flat-panel displays or microplasma-based devices.

## AUTHOR INFORMATION

### Corresponding Authors

*E-mail: nhtai@mx.nthu.edu.tw (N.-H.T.).
*E-mail: inanlin@mail.tku.edu.tw (I.-N.L.).

### Notes

The authors declare no competing financial interest.

## ACKNOWLEDGMENTS

The authors would like to thank the National Science Council, Taiwan, Republic of China, for the support of this research through the project Nos. NSC 101-2221-E-007-064-MY3 and NSC102-2112-M032-006.

## REFERENCES

(1) Ijima, S. Helical Microtubules of Graphitic Carbon. *Nature* **1991**, *354*, 56−58.
(2) Huang, C. S.; Yeh, C. Y.; Chang, Y. H.; Hsieh, Y. M.; Ku, C. Y.; Lai, Q. T. Field Emission Properties of CNT−ZnO Composite Materials. *Diamond Relat. Mater.* **2009**, *18*, 452−456.
(3) DeHeer, W. A.; Châtelain, A.; Ugarte, D. A Carbon Nanotube Field-Emission Electron Source. *Science* **1995**, *270*, 1179−1180.
(4) Cheng, Y.; Zhou, O. Electron Field Emission from Carbon Nanotubes. *C. R. Phys.* **2003**, *4*, 1021−1033.
(5) Lysenkov, D.; Muller, G. Field Emission Measurement Techniques for the Optimisation of Carbon Nanotube Cathodes. *Int. J. Nanotechnol.* **2005**, *2*, 239−254.
(6) Dean, K. A.; Burgin, T. P.; Chalamala, B. R. Evaporation of Carbon Nanotubes during Electron Field Emission. *Appl. Phys. Lett.* **2001**, *79*, 1873−1875.
(7) Dean, K. A.; Chalamala, B. R. The Environmental Stability of Field Emission from Single-Walled Carbon Nanotubes. *Appl. Phys. Lett.* **1999**, *75*, 3017−3019.
(8) Green, J. M.; Dong, L.; Gutu, T.; Jiao, J.; Conley, J. F.; Ono, J. Y. ZnO-Nanoparticle-Coated Carbon Nanotubes Demonstrating Enhanced Electron Field-Emission Properties. *J. Appl. Phys.* **2006**, *99*, 094308.
(9) Sharma, H.; Kaushik, V.; Girdhar, P.; Singh, V. N.; Shukla, A. K.; Vankar, V. D. Enhanced Electron Emission from Titanium Coated Multiwalled Carbon Nanotubes. *Thin Solid Films* **2010**, *518*, 6915−6920.
(10) Zou, Y.; May, P. W.; Vieira, S. M. C.; Fox, N. A. Field Emission from Diamond-Coated Multiwalled Carbon Nanotube "Teepee" Structures. *J. Appl. Phys.* **2012**, *112*, 044903.
(11) Fiori, A.; Orlanducci, S.; Sessa, V.; Tamburri, E.; Toschi, F.; Terranova, M. L.; Ciorba, A.; Rossi, M.; Lucci, M.; Barnard, A. S. Hybrid Carbon Nanotube/Nanodiamond Structures as Electron Emitters for Cold Cathodes. *J. Nanosci. Nanotechnol.* **2008**, *8*, 1989−1993.
(12) Lee, D. H.; Lee, J. A.; Lee, W. J.; Choi, D. S.; Lee, W. J.; Kim, S. O. Facile Fabrication and Field Emission of Metal-Particle-Decorated Vertical N-Doped Carbon Nanotube/Graphene Hybrid Films. *J. Phys. Chem. C* **2010**, *114*, 21184−21189.
(13) Mauricio Rosolen, J.; Tronto, S.; Marchesin, M. S.; Almeida, E. C.; Ferreira, N. G.; Patrick Poá, C. H.; Silva, S.; Ravi, P. Electron Field Emission from Composite Electrodes of Carbon Nanotubes-Boron-Doped Diamond and Carbon Felts. *Appl. Phys. Lett.* **2006**, *88*, 083116.
(14) Varshney, D.; Ahmadi, M.; Guinel, M. J. F.; Weiner, B. R.; Morell, G. Single-Step Route to Diamond-Nanotube Composite. *Nanoscale Res. Lett.* **2012**, *7*, 535.
(15) Sankaran, K. J.; Srinivasu, K.; Chen, H. C.; Dong, C. L.; Leou, K. C.; Lee, C. Y.; Tai, N. H.; Lin, I. N. Improvement in Plasma Illumination Properties of Ultrananocrystalline Diamond Films by Grain Boundary Engineering. *J. Appl. Phys.* **2013**, *114*, 054304.
(16) Bozeman, S. P.; Baumann, P. K.; Ward, B. L.; Powers, M. J.; Cuomo, J. J.; Nemanich, R. J.; Dreifus, D. L. Electron Emission Measurements from CVD Diamond Surfaces. *Diamond Relat. Mater.* **1996**, *5*, 802−806.
(17) Sowers, A. T.; Ward, B. L.; English, S. L.; Nemanich, R. J. Field Emission Properties of Nitrogen-Doped Diamond Films. *J. Appl. Phys.* **1999**, *86*, 3973−3982.
(18) Shankar, N.; Glumac, N. G.; Yu, M. F.; Vanka, S. P. Growth of Nanodiamond/Carbon-Nanotube Composites with Hot Filament Chemical Vapor Deposition. *Diamond Relat. Mater.* **2008**, *17*, 79−83.
(19) Sun, L. T.; Gong, J. L.; Zhu, Z. Y.; Zhu, D. Z.; He, S. X.; Wang, Z. X.; Chen, Y.; Hu, G. Nanocrystalline Diamond from Carbon Nanotubes. *Appl. Phys. Lett.* **2004**, *84*, 2901−2903.
(20) Xiao, X. C.; Elam, J. W.; Trasobares, S.; Auciello, O.; Carlisle, J. A. Synthesis of a Self-Assembled Hybrid of Ultrananocrystalline Diamond and Carbon Nanotubes. *Adv. Mater.* **2005**, *17*, 1496−1500.
(21) Chang, T. H.; Panda, K.; Panigrahi, B. K.; Lou, S. C.; Chen, C.; Chan, H. C.; Lin, I. N.; Tai, N. H. Electrophoresis of Nanodiamond on the Growth of Ultrananocrystalline Diamond Films on Silicon Nanowires and the Enhancement of the Electron Field Emission Properties. *J. Phys. Chem. C* **2012**, *116*, 19867−19876.
(22) Fowler, R. H.; Nordheim, L. Electron Emission in Intense Electric Fields. *Proc. R. Soc. London, Ser. A* **1928**, *119*, 173−181.
(23) Wang, C. S.; Chen, H. C.; Cheng, H. F.; Lin, I. N. Synthesis of Diamond using Ultra-Nanocrystalline Diamonds as Seeding Layer and Their Electron Field Emission Properties. *Diamond Relat. Mater.* **2009**, *18*, 136−140.
(24) Cheng, H. F.; Chiang, H. Y.; Horng, C. C.; Chen, H. C.; Wang, C. S.; Lin, I. N. Enhanced Electron Field Emission Properties by Tuning the Microstructure of Ultrananocrystalline Diamond Film. *J. Appl. Phys.* **2011**, *109*, 033711.
(25) Sun, Z.; Shi, J. R.; Tay, B. K.; Lau, S. P. UV Raman Characteristics of Nanocrystalline Diamond Films with Different Grain Size. *Diamond Relat. Mater.* **2000**, *9*, 1979−1983.
(26) Ferrari, A. C.; Robertson, J. Origin of the 1150−$cm^{-1}$ Raman Mode in Nanocrystalline Diamond. *Phys. Rev. B* **2001**, *63*, 121405.
(27) Michler, J.; von Kaenel, Y.; Stiegler, J.; Blank, E. Complementary Application of Electron Microscopy and Micro-Raman Spectroscopy for Microstructure, Stress, and Bonding Defect Investigation of Heteroepitaxial Chemical Vapor Deposited Diamond Films. *J. Appl. Phys.* **1998**, *83*, 187−197.

(28) Konyashin, I.; Zern, A.; Mayer, J.; Aldinger, F.; Babaev, V.; Khvostov, V.; Guseva, M. A New Carbon Modification: 'n-diamond' or Face-Centred Cubic Carbon? *Diamond Relat. Mater.* **2001**, *10*, 99−102.
(29) Konyashin, I.; Khvostov, V.; Babaev, V.; Guseva, M.; Mayer, J.; Sirenko, A. A New Hard Allotropic Form of Carbon: Dream or Reality? *Int. J. Refract. Met. Hard Mater.* **2006**, *24*, 17−23.
(30) Prawer, S.; Peng, J. L.; Orwa, J. O.; McCallum, J. C.; Jamieson, D. N.; Bursill, L. A. Size Dependence of Structural Stability in Nanocrystalline Diamond. *Phys. Rev. B* **2000**, *62*, 16360−16363.
(31) Arenal, R.; Bruno, P.; Miller, D. J.; Bleuel, M.; Lal, J.; Gruen, D. M. Diamond Nanowires and the Insulator-Metal Transition in Ultrananocrystalline Diamond Films. *Phys. Rev. B* **2007**, *75*, 195431.
(32) Gruen, D. M.; Liu, S.; Krauss, A. R.; Luo, J.; Pan, X. Fullerenes as Precursors for Diamond Film Growth without Hydrogen or Oxygen Additions. *Appl. Phys. Lett.* **1994**, *64*, 1502−1504.
(33) Kovarik, P.; Bourdon, E. B. D.; Prince, R. H. Electron-Energy-Loss Characterization of Laser-Deposited *a*-C, *a*-C:H, and Diamond Films. *Phys. Rev. B* **1993**, *48*, 12123−12129.
(34) Raizer, Y. P.; Allen, J. E.; Kisin, V. I. *Gas Discharge Physics*, 1st ed.; Springer-Verlag Publications: New York, 1991.
(35) Sankaran, K. J.; Panda, K.; Sundaravel, B.; Chen, H. C.; Lin, I. N.; Lee, C. Y.; Tai, N. H. Engineering the Interface Characteristics of Ultrananocrystalline Diamond Films Grown on Au-Coated Si Substrates. *ACS Appl. Mater. Interfaces* **2012**, *4*, 4169−4176.
(36) Chen, H. C.; Sankaran, K. J.; Lou, S. C.; Lin, L. J.; Tai, N. H.; Lee, C. Y.; Lin, I. N. Using an Au Interlayer to Enhance Electron Field Emission Properties of Ultrananocrystalline Diamond Films. *J. Appl. Phys.* **2012**, *112*, 103711.
(37) Lieberman, M. A.; Lichtenberg, A. J. *Principles of Plasma Discharges and Materials Processing*, 2nd ed.; Wiley Interscience, John Wiley & Sons, Inc. Publications: Hoboken, NJ, 2005.